Catalysis Today 153 (2010) 143–149

Contents lists available at ScienceDirect

Catalysis Today

journal homepage: www.elsevier.com/locate/cattod

# Hydrothermal synthesis and catalytic performance of single-crystalline $La_{2-x}Sr_xCuO_4$ for methane oxidation

Lei Zhang, Yue Zhang, Hongxing Dai*, Jiguang Deng, Li Wei, Hong He*

*Laboratory of Catalysis Chemistry and Nanoscience, Department of Chemistry and Chemical Engineering, College of Environmental and Energy Engineering, Beijing University of Technology, Beijing 100124, PR China*

ARTICLE INFO

*Article history:*
Available online 3 April 2010

*Keywords:*
Perovskite-like oxide catalyst
Single-crystalline strontium-substituted lanthanum cuprate
Hydrothermal synthesis
Microrod-like morphology
Methane combustion

ABSTRACT

The microsized perovskite-like oxide $La_{2-x}Sr_xCuO_4$ ($x = 0, 1$) single crystallites with a rod-like morphology were fabricated with KOH as the alkaline source at a hydrothermal temperature of 180–260 °C and after calcination at 850 °C, and characterized by means of the XRD, BET, SEM, SAED (selected area electron diffraction), $O_2$-TPD, and $H_2$-TPR techniques. The catalytic performance of the materials was evaluated for methane combustion. It is shown that (i) the single-crystalline cuprate catalyst outperformed its polycrystalline counterpart; (ii) the doping of $Sr^{2+}$ to the $La_2CuO_4$ lattice enhanced the catalytic activity; (iii) the $LaSrCuO_4$ catalyst fabricated with 12 mol/L KOH as the alkaline source at a hydrothermal temperature of 260 °C showed the best performance (the temperature for 90% $CH_4$ conversion = 667 °C) for methane combustion at $CH_4/O_2$ molar ratio = 1/10 and SV = 50,000 mL/(g h); and (iv) there was a clear relationship between the α-oxygen desorption or reducibility and catalytic activity. It is concluded that the more adsorbed oxygen species, better reducibility, single crystallinity, and unique morphology are responsible for the excellent performance of the $LaSrCuO_4$ single crystallite in catalyzing the combustion of methane.



## 1. Introduction

It is well known that noble metals, transition metal oxides, and mixed metal oxides (e.g. perovskite-type oxides and perovskite-like oxides) are good catalysts for the combustion of light hydrocarbons. Due to the high cost and easy sintering of noble metals at high temperatures [1], their wide catalytic applications are limited. Among the base metal-based catalysts, perovskite-type and perovskite-like oxides exhibit promising performance in catalyzing the combustion of methane. Moreover, the latter display better thermal stability than the former [2,3], and hence are more suitable for the use as catalyst in the high-temperature reactions.

Perovskite-like oxides are usually prepared via the solid-state reaction [4] and citric acid complexing routes [5]. These materials obtained by means of the above methods are polycrystalline. In recent years, single-crystalline perovskites have been reported to be successfully fabricated adopting hydrothermal strategies. Hydrothermal processing is an effective technique for the generation of nano- or microsized mixed oxides at low temperatures [6]. Hydrothermal conditions, such as precursor nature and concentration, pH value, temperature, and time, have critical impacts on the crystal structure and morphology of the product [7]. So far, a large number of works have reported successful fabrication of perovskites with specific surface morphologies, which show advantageous physicochemical behaviors over their conventional irregular counterparts. For example, single-crystalline $BaTiO_3$ nanocubes and $BaTiO_3/SrTiO_3$ microspheres could be synthesized hydrothermally at 165–220 °C [8] and at 180 °C [9], respectively, and these regularly morphological materials exhibited promising applications in catalysis, ferroelectrics, and photoelectrics. However, single-crystalline perovskite-related materials are rarely employed as catalyst. Recently, Zhu and coworkers investigated strontium-substituted lanthanum manganite catalysts derived from a hydrothermal process for the oxidation of CO and $CH_4$, and observed that the cube-like single-crystal materials possessed better catalytic performance and thermal stability than their irregularly morphological polycrystalline nanoparticles [10]. Therefore, it is highly desirable to investigate the fabrication and catalytic behaviors of perovskite-related oxides with single-crystalline structures for the combustion of hydrocarbons.

In the past years, we have generated numerous perovskite-type and perovskite-like oxides using citric acid complexing and/or hydrothermal method, and studied their catalytic properties for the oxidation of carbon monoxide [11,12], light hydrocarbons [13,14], and volatile organic compounds [15,16]. Recently, we have obtained single-crystalline $La_{0.6}Sr_{0.4}CoO_3$ nanowires/nanorods and $La_{1-x}Sr_xMnO_3$ ($x = 0.4$, 0.5, 0.6) microcubes via hydrothermal routes, and found that the single-crystalline perovskite-type oxides

* Corresponding authors. Tel.: +86 10 6739 6588; fax: +86 10 6739 1983.
*E-mail addresses:* hxdai@bjut.edu.cn (H. Dai), hehong@bjut.edu.cn (H. He).

0920-5861/$ – see front matter © 2010 Elsevier B.V. All rights reserved.
doi:10.1016/j.cattod.2010.02.059

outperformed their polycrystalline counterparts for toluene combustion [15,17]. Very recently, we have extended our attention to the catalysis of single-crystalline perovskite-like oxides in the oxidation of hydrocarbons. Here, we report the hydrothermal fabrication, characterization, and catalytic performance of $La_{2-x}Sr_xCuO_4$ single crystallites with specific morphologies for methane combustion.

## 2. Experimental

### 2.1. Catalyst fabrication

The $La_{2-x}Sr_xCuO_4$ ($x = 0, 1$) catalysts were fabricated by adopting the hydrothermal strategy. In a typical fabrication, stoichiometric amounts of nitrates of La and Cu for $La_2CuO_4$ (denoted as LCO) or nitrates of La, Sr, and Cu for $LaSrCuO_4$ (denoted as LSCO) were mixed with 30 mL of deionized (DI) water under stirring and ultrasonic irradiation. Then, a potassium hydroxide aqueous solution (9, 12 or 15 mol/L) was added dropwise until the pH value of the mixed solution reached 13 or above for complete co-precipitation. The co-precipitation solution was transferred to the 50-mL Teflon-lined stainless steel autoclave for hydrothermal treatment at 180, 220 or 260 °C for 48 h. After the mixture was cooled down to room temperature (RT) and dried at 60 °C for 12 h, we calcined the solid in air at a heating rate of 1 °C/min from RT to 400 °C and kept at this temperature for 1 h, and then continuously heated at a ramp of 3 °C/min to 850 °C and maintained at 850 °C for 6 h. For better presentation, we used LCO_*X*M-*Y* or LSCO_*X*M-*Y* to represent the LCO or LSCO catalyst fabricated with *X* mol/L (*X* = 9, 12, 15) KOH as the alkaline source at a hydrothermal temperature of *Y* °C (*Y* = 180, 220, 260). For comparison purposes, we also prepared the polycrystalline LCO and LSCO catalysts (denoted as LCO_Citrate and LSCO_Citrate, respectively) using the citric acid complexing method [18] and the catalysts were calcined in air at 950 °C for 6 h.

All of the chemicals (analytical grade) were purchased from the Beijing Chemical Regent Company and used without further purification.

### 2.2. Catalyst characterization

The crystal structures of the catalysts were determined on an X-ray diffractometer (Bruker/AXS D8 Advance) operating at 35 kV and 35 mA using Cu Kα irradiation and nickel filter (λ = 0.15406 nm). The patterns recorded were referred to the JCPDS Database for phase identification. BET (Brunauer–Emmett–Teller) surface areas of the catalysts were measured via $N_2$ adsorption at −196 °C on a Micromeritics ASAP 2020 apparatus with the samples outgassed at 300 °C for 0.5 h under vacuum before measurement. The scanning electron microscopic (SEM) images of the catalysts were recorded on a FEI Quanta 200 apparatus (operating at 30 kV). The selected area electron diffraction (SAED) patterns of the catalysts were obtained by means of a JEOL-2010 instrument (operating at 200 kV). X-ray photoelectron spectroscopy (XPS, VG CLAM 4 MCD analyzer) was employed to determine the La 3d, Sr 2p, Cu 2p, O 1s, and C 1s binding energies (BEs) of surface species with Mg Kα (hν = 1253.6 eV) as the excitation source. The instrumental resolution was 0.5 eV. Before XPS determination, the catalysts were calcined in $O_2$ (flow rate, 20 mL/min) at 600 °C for 1 h and then cooled to RT. After such a pretreatment, the catalysts were mounted and transferred to the spectrometer in a transparent Glove Bag (Instruments for Research and Industry, USA) filled with helium. The samples were then outgassed in the preparation chamber ($10^{-5}$ Torr) for 0.5 h and introduced into the analysis chamber ($3 \times 10^{-9}$ Torr) for recording. The C 1s peak at 284.6 eV was taken as a reference for BE calibration.

Hydrogen temperature-programmed reduction ($H_2$-TPR) experiments were conducted on a Micromeritics Autochem II 2920 chemical adsorption apparatus. The catalyst (0.1 g, 40–60 mesh) was first pretreated in helium (flow rate = 30 mL/min) at 300 °C for 0.5 h in a quartz fixed-bed U-shaped micro-reactor (i.d. = 4 mm). After cooling to RT in the same atmosphere, the catalyst was exposed to a flow (50 mL/min) of 5% $H_2$–95% Ar (v/v) mixture and heated at a rate of 15 °C/min to 900 °C. The change in $H_2$ concentration of the outlet gases was monitored on-line on a chemical adsorption apparatus. The signal peak was calibrated against that of the complete reduction of a known standard of powder CuO (Aldrich, 99.995%).

For the $O_2$ temperature-programmed desorption ($O_2$-TPD) studies, the catalyst (0.1 g, 40–60 mesh) was placed in the middle of a quartz micro-reactor (i.d. = 4 mm). The outlet gases were analyzed on-line by a mass spectrometer (Hiden HPR20). Before each run, the catalyst was treated in $O_2$ (flow rate = 30 mL/min) at 700 °C for 0.5 h, followed by cooling in $O_2$ to RT and helium purging (flow rate = 50 mL/min) for 3 h for the total removal of gas-phase oxygen in the system. The pretreated catalyst was heated (10 °C/min) from RT to 900 °C. The amount of $O_2$ desorbed from the catalyst was quantified by calibrating the peak area against that of a standard oxygen pulse (50.0 μL).

### 2.3. Activity measurements

Catalytic evaluation was conducted in a continuous flow fixed-bed quartz micro-reactor (i.d. = 4 mm) at atmospheric pressure. 0.1 g of the catalyst (40–60 mesh) and equal amount of quartz sand (40–60 mesh) were well mixed and loaded into the micro-reactor. The volumetric composition of the reactant mixture was 2% $CH_4$ + 20% $O_2$ + 78% $N_2$ (balance), giving a space velocity (SV) of 50,000 mL/(g h). The outlet gases were analyzed on-line by gas chromatography (GC-14C, Shimadzu) equipped with a thermal conductivity detector and a 5A molecular sieve column. Based on the data of methane conversion (Methane *conv.*), methane flow rate ($F_{CH_4}$), and catalyst mass ($m_{cat.}$), one can calculate the $CH_4$ reaction rate according to the following formulas:

$$\text{Methane } conv.\ (\%) = \frac{C_0 - C_i}{C_0} \times 100$$

$$CH_4 \text{ reaction rate } (\text{mmol}/(\text{g h})) = \frac{\text{Methane } conv. \times F_{CH_4}}{m_{cat.} \times 22.4}$$

where $C_0$ and $C_i$ is the initial methane concentration and the methane concentration at a reaction temperature ($T_i$) and a reaction time ($t_i$), respectively. The balance of carbon throughout the catalytic system was evaluated to be 99.5%.

## 3. Results and discussion

### 3.1. Crystal phase compositions

Fig. 1 illustrates the powder XRD patterns of the LCO and LSCO catalysts fabricated with different KOH concentrations and at hydrothermal temperatures. By referring to the XRD patterns of the standard $La_2CuO_4$ (JCPDS PDF# 82-2142) and $LaSrCuO_4$ (JCPDS PDF# 71-1523) samples, one can deduce that the as-fabricated LCO and LSCO (as well as LCO_Citrate and LSCO_Citrate, not shown here) catalysts were of orthorhombic and tetragonal perovskite-like structures, respectively; no diffraction peaks attributable to impurity phases were detected in LSCO_12M-260, indicating that this Sr-substituted catalyst was single phase. However, there was

**Table 1**
Surface $O_{ads}/O_{latt}$ and $Cu^{3+}/Cu^{2+}$ molar ratios, $O_2$ desorptions, and $H_2$ consumptions, and performance of the catalysts for methane combustion.

| Catalyst | XPS[a] | | $O_2$-TPD | | $H_2$-TPR | | Catalytic activity[b] | | | BET surface area ($m^2/g$) |
|---|---|---|---|---|---|---|---|---|---|---|
| | $O_{ads}/O_{latt}$ | $Cu^{3+}/Cu^{2+}$ | $T_\alpha$ (°C)/$O_2$ desorption (μmol/g) | $T_\beta$ (°C)/$O_2$ desorption (μmol/g) | $T_\alpha$ (°C)/$H_2$ consumption (mmol/g) | $T_\beta$ (°C)/$H_2$ consumption (mmol/g) | $T_{10\%}$ (°C) | $T_{50\%}$ (°C) | $T_{90\%}$ (°C) | |
| LCO_12M-260 | 2.97 | 0.137 | 390/45.5 | 891/85.0 | 278/1.69 | 412/1.28 | 548 | 662 | 739 | 3.6 |
| LCO_12M-220 | 2.18 | 0.135 | 423/29.4 | –/– | 319/1.57 | 423/1.31 | 587 | 677 | 759 | 4.3 |
| LCO_12M-180 | 1.93 | 0.116 | 410/21.2 | –/– | 321/1.44 | 429/1.09 | 625 | 722 | 766 | 7.2 |
| LSCO_12M-260 | 4.53 | 0.389 | 404/143.0 | (833, 886)/179.6 | 226/1.16 | 394/2.70 | 482 | 620 | 667 | 11.9 |

[a] $O_{ads}/O_{latt}$ and $Cu^{3+}/Cu^{2+}$ denote the molar ratio of surface adsorbed oxygen ($O_{ads}$) and lattice oxygen ($O_{latt}$) species and surface $Cu^{3+}$ and $Cu^{2+}$ species in the catalyst, respectively.
[b] $T_{10\%}$, $T_{50\%}$, and $T_{90\%}$ denotes the reaction temperature at a methane conversion of 10, 50, and 90%, respectively.

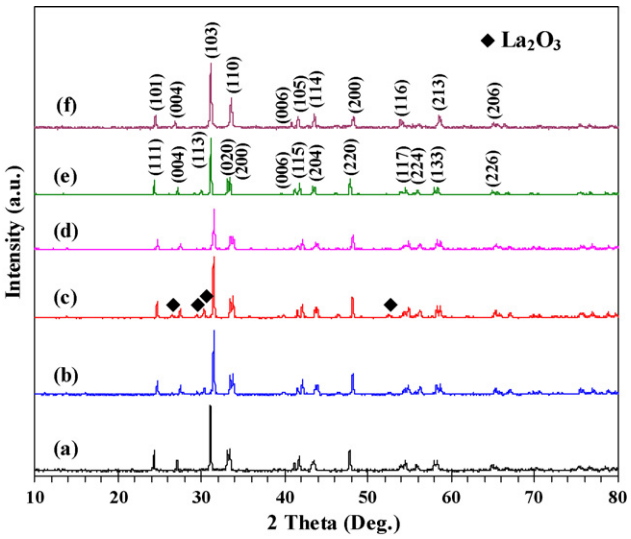


**Fig. 1.** XRD patterns of (a) LCO_12M-260, (b) LCO_12M-220, (c) LCO_12M-180, (d) LCO_9M-260, (e) LCO_15M-260, and (f) LSCO_12M-260.

presence of a trace amount of $La_2O_3$ impurity phase (JCPDS PDF# 83-1355) in the LCO_12M-220 and LCO_12M-180 catalysts, suggesting that a lower hydrothermal temperature was not favorable for the formation of single-phase perovskite-like oxides. All of the diffraction peaks could be well indexed, as indicated in Fig. 1(e) and (f). It should be noted that no substantial amounts of perovskite-like oxide phases were generated in the solids obtained after the direct hydrothermal process (without DI water washing and calcination at high temperatures) or after DI water washing before calcination at 850 °C. Therefore, high-temperature calcination and no DI water washing are two important steps in preparing such structural materials.

### 3.2. Catalyst particle morphologies

Fig. 2 shows the SEM images as well as the typical SAED patterns of the LCO_12M-180, LCO_12M-260, LCO_15M-260, LSCO_12M-260, and LSCO_Citrate. The appearance of well-lined array of bright electron diffraction spots in the SAED patterns (insets of Fig. 2(a) and (d)) indicates the formation of well-grown LCO and LSCO single crystallites, similar single-crystal structures also existed in the other hydrothermally fabricated catalysts (not shown here). However, the LCO_Citrate and LSCO_Citrate catalysts possessed a polycrystalline structure, as revealed by the recording of multiple bright electron diffraction rings (insets of Fig. 2(e) and (f)). From Fig. 2, one can observe that the LCO and LSCO catalysts derived from hydrothermal treatments displayed a microrod-like morphology, with the diameter and length of 300–800 nm and 3–8 μm, respectively. An alteration in KOH concentration or hydrothermal temperature did not induce a significant change in particle morphology of the LCO or LSCO product. The only differences between the LCO or LSCO catalysts were the particle size (Fig. 2) and crystallinity (Fig. 1). These results indicate that rod-like LCO or LSCO catalysts could be generated under the hydrothermal and calcination conditions adopted in the present study. From Table 1, one can see that the obtained microrod-like LCO and LSCO catalysts showed lower surface areas (3.6–11.9 $m^2/g$), a result due to their calcination at a high temperature. As for the LCO_Citrate and LSCO_Citrate catalysts, there was an aggregation of irregularly morphological microsized particles (Fig. 2(e) and (f)), giving a surface area of 2.1 and 2.4 $m^2/g$, respectively.

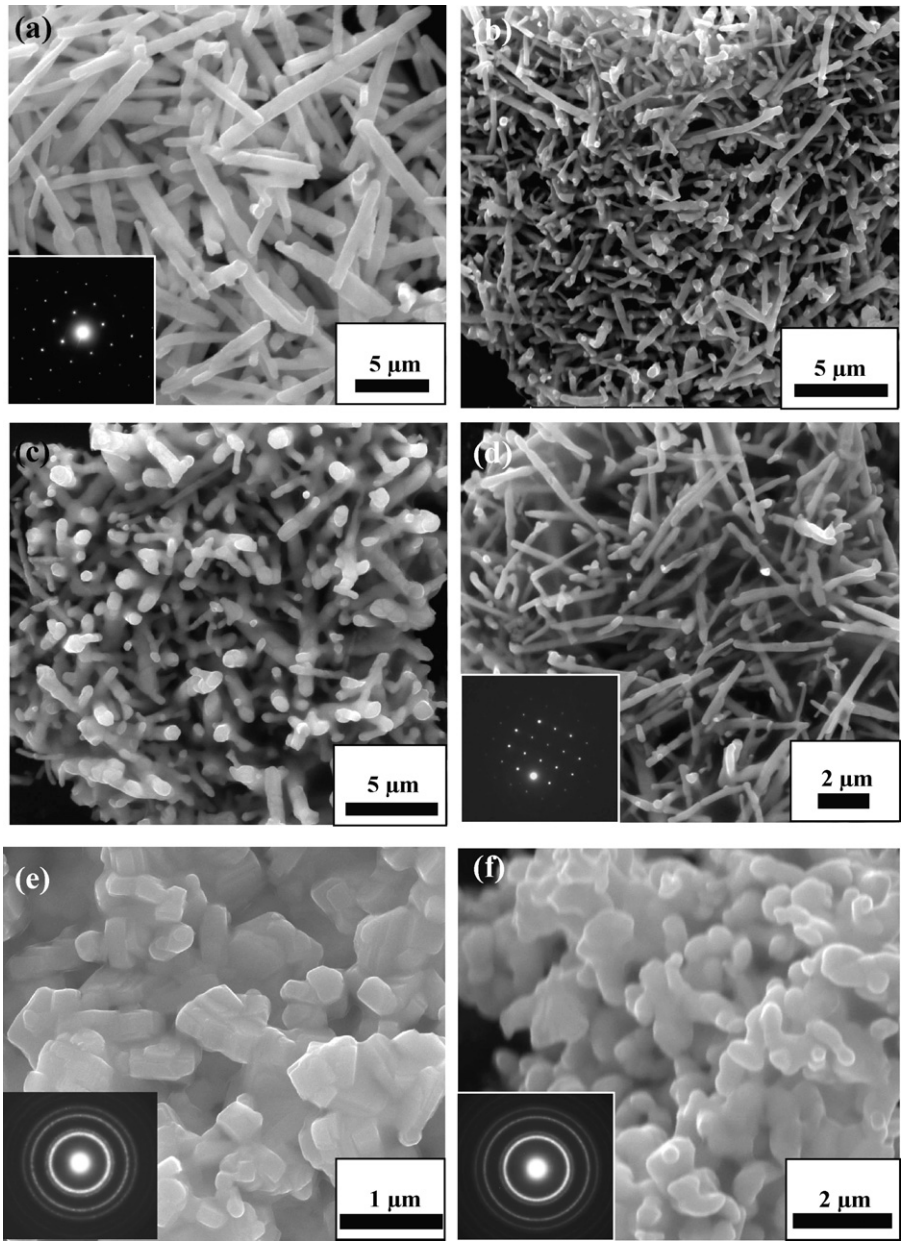


**Fig. 2.** SEM images and SAED patterns (insets) of (a) LCO_12M-260, (b) LCO_12M-180, (c) LCO_15M-260, (d) LSCO_12M-260, (e) LCO_Citrate, and (f) LSCO_Citrate.

### 3.3. Surface oxygen species and copper oxidation states

Fig. 3 illustrates the O 1s and Cu $2p_{3/2}$ XPS spectra of the LCO and LSCO catalysts. We used the curve-fitting strategy to decompose these spectra. From Fig. 3A, one can observe two components at BE = ca. 528.7 and 531.5 eV in the O 1s spectrum of each catalyst, which could be attributed to the surface lattice oxygen ($O_{latt}$) and adsorbed oxygen ($O_{ads}$, e.g. $O^-$, $O_2^{2-}$, $O_2^-$ or surface hydroxyl) species [19], respectively. Since the catalysts were pretreated in an $O_2$ flow at 600 °C and transferred to the spectrometer chamber without exposure to the air before the recording of XPS spectra, one can preclude the possibility of surface hydroxyl species existence. It has been generally accepted that adsorbed oxygen species are usually located at the surface oxygen vacancy sites of perovskites [13,20]. Therefore, the $O_{ads}$ amount is closely associated with the oxygen vacancy density. The higher the oxygen vacancy density is, the easier the $O_{ads}$ is formed during oxidation reaction [21]. From the Cu $2p_{3/2}$ XPS spectra of the four cuprate catalysts (Fig. 3B), one can observe an asymmetrical main peak at BE = ca. 934 eV and shake-up satellite peaks in the BE range of 939–946 eV. The main peak could be decomposed into two components at BE = ca. 933.5 and 934.6 eV, assignable to $Cu^{2+}$ (together with the appearance of shake-up satellites) [13] and $Cu^{3+}$ [13,22], respectively. The surface $O_{ads}/O_{latt}$ and $Cu^{3+}/Cu^{2+}$ molar ratios, $O_2$ desorptions, $H_2$ consumptions as well as activities of the catalysts are summarized in Table 1. Apparently, the surface $O_{ads}/O_{latt}$ molar ratio decreased in the sequence of LSCO_12M-260 > LCO_12M-260 > LCO_12M-220 > LCO_12M-180, in good agreement with the order of their catalytic performance (shown in Section 3.5). The partial replacement of $La^{3+}$ by $Sr^{2+}$ would regulate the oxidation state distribution of copper ions and hence enhance the oxygen vacancy density, therefore giving rise to an augmentation in $O_{ads}$ concentration. With the rise in hydrothermal temperature, the $O_{ads}/O_{latt}$ molar ratio also increased, indicating that a higher hydrothermal temperature favored the increase in oxygen vacancy density. The surface $Cu^{3+}/Cu^{2+}$ molar ratio in the LSCO_12M-260 catalyst was

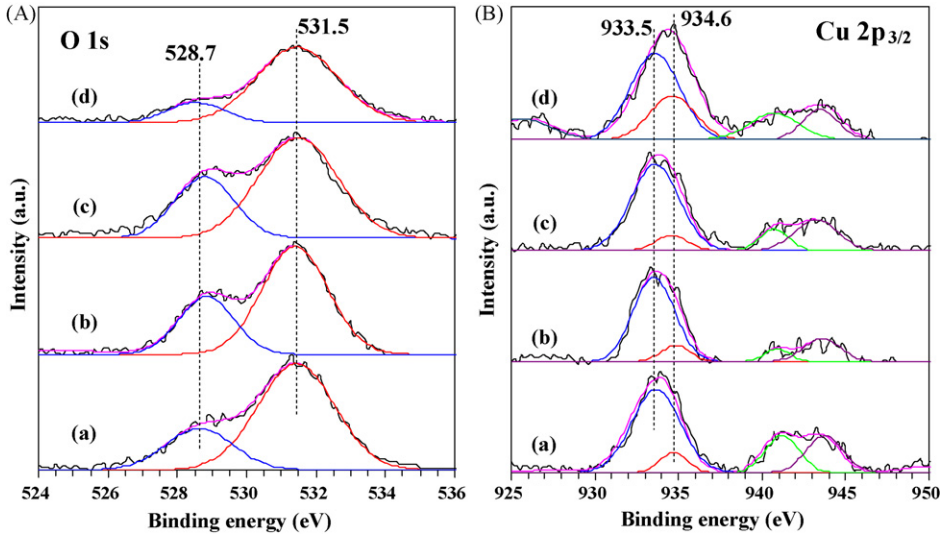


**Fig. 3.** (A) O 1s and (B) Cu $2p_{3/2}$ XPS spectra of (a) LCO_12M-260, (b) LCO_12M-220, (c) LCO_12M-180, and (d) LSCO_12M-260.

much higher than those in the LCO catalysts (Table 1), a result due to the partial substitution of $La^{3+}$ by $Sr^{2+}$.

$O_2$-TPD is an effective technique to investigate the oxygen desorption behaviors of mixed oxide catalysts. Usually, desorption of methane is much smaller than that of oxygen from perovskite-type and perovskite-like oxides [23]. Fig. 4 shows the $O_2$-TPD profiles of the cuprate catalysts. It is seen that there were two kinds of oxygen desorption at low temperature (below 600 °C) and high temperature (above 600 °C), in which the low-temperature desorption (called α-oxygen desorption) could be attributed to the adsorbed oxygen species at oxygen vacancies, whereas the high-temperature desorption (called β-oxygen desorption) could be assigned to the lattice oxygen. The desorption of β-oxygen involves the reduction of $Cu^{3+}$ and $Cu^{2+}$ to $Cu^0$ [24,25]. It is believed that α-oxygen is active species in methane combustion [26], although β-oxygen acts as a promotional role on such an oxidation process [27]. By quantifying the $O_2$-TPD peaks, one can realize that the α-oxygen desorption decreased in the order of LSCO_12M-260 ≫ LCO_12M-260 > LCO_12M-220 > LCO_12M-180, coinciding with the sequence of their catalytic performance (Table 1).

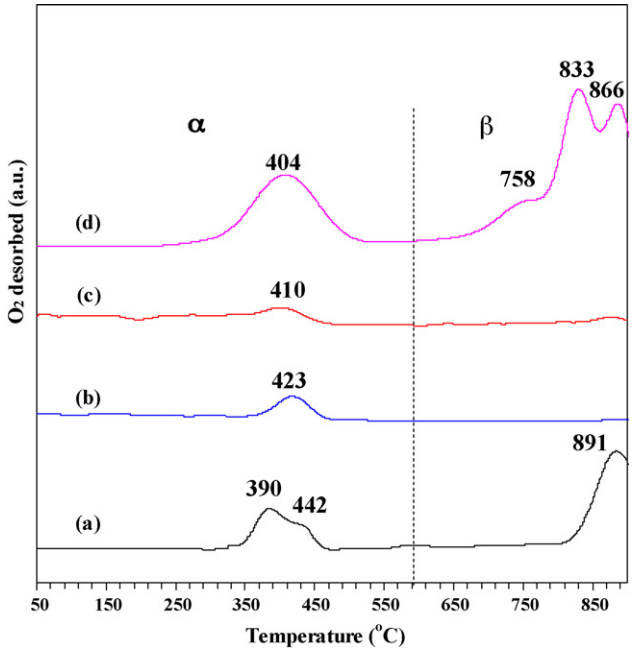


**Fig. 4.** $O_2$-TPD profiles of (a) LCO_12M-260, (b) LCO_12M-220, (c) LCO_12M-180, and (d) LSCO_12M-260.

### 3.4. Reducibility

Fig. 5 illustrates the $H_2$-TPR profiles and corresponding initial $H_2$ consumption rates of the LCO and LSCO catalysts. It is observed from Fig. 5A that there were two reduction bands for each catalyst, with the Sr-substituted catalyst (a third reduction band appeared at 759 °C) being the exception. In each profile, the first reduction band is called α-reduction whereas the second one β-reduction. Obviously, the LSCO_12M-260 catalyst could be reduced at lower temperatures as compared to the LCO catalysts. In other words, the Sr-doped lanthanum cuprate catalyst possessed the best reducibility. The α- and β-reductions were due to the stepwise reduction of surface and bulk $Cu^{3+}$ and $Cu^{2+}$ species in different local coordination environments [18,28]. The total $H_2$ consumption (3.86 mmol/g) below 550 °C of the LSCO_12M-260 catalyst was much higher than those (2.53–2.97 mmol/g) of the three LCO catalysts. Supposing that all of the copper ions in $La_2CuO_4$ (or $LaSrCuO_4$) existed in divalency and in trivalency, the $H_2$ consumption would be 2.47 and 3.70 mmol/g (or 2.82 and 4.24 mmol/g), respectively. Apparently, the total $H_2$ consumption of each of the as-fabricated LCO or LSCO catalysts fell into the above range. This result suggests that $Cu^{3+}$ and $Cu^{2+}$ co-existed in the LCO and LSCO catalysts, in good concordance with the results of XPS investigations. Initial $H_2$ consumption rate per gram (or per mole) of a material when reduction is less than 20% (i.e., before the occurrence of phase transformation) is a good parameter to evaluate its reducibility. Fig. 5B shows the initial $H_2$ consumption rates of the LCO and LSCO catalysts. It is clearly seen that the initial $H_2$ consumption rate decreased in the order of LSCO_12M-260 ≫ LCO_12M-260 > LCO_12M-220 > LCO_12M-180. That is to say, their corresponding reducibility also followed such a sequence, same as the order in catalytic activity of these materials.

### 3.5. Catalytic performance

In the blank experiment, no significant activity was observed below 770 °C over the quartz sands. It means that methane

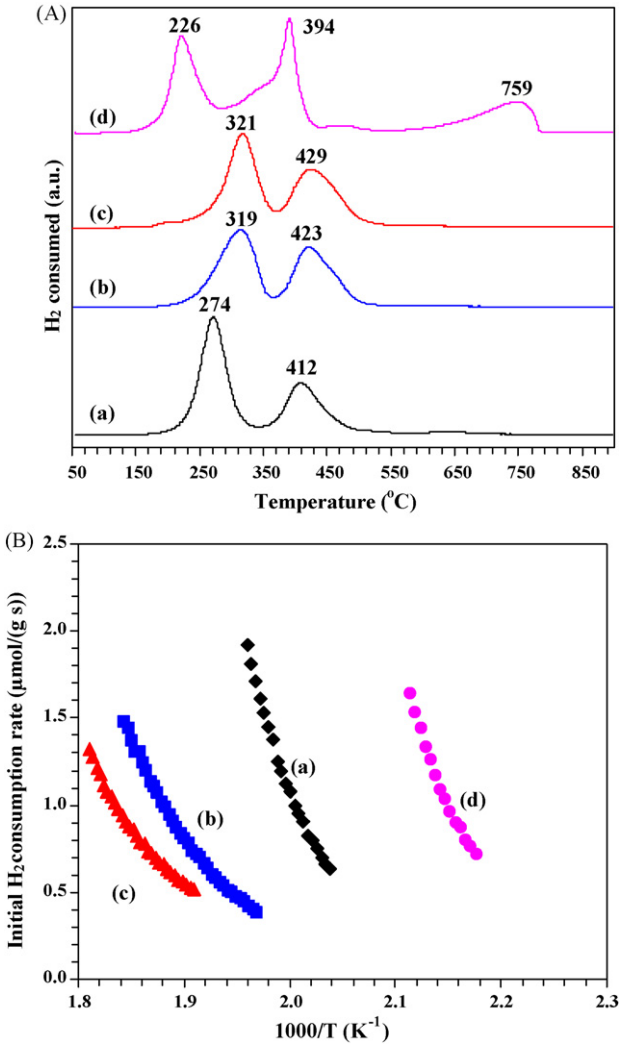


**Fig. 5.** (A) $H_2$-TPR profiles and (B) initial $H_2$ consumption rate versus inverse temperature of (a) LCO_12M-260, (b) LCO_12M-220, (c) LCO_12M-180, and (d) LSCO_12M-260.

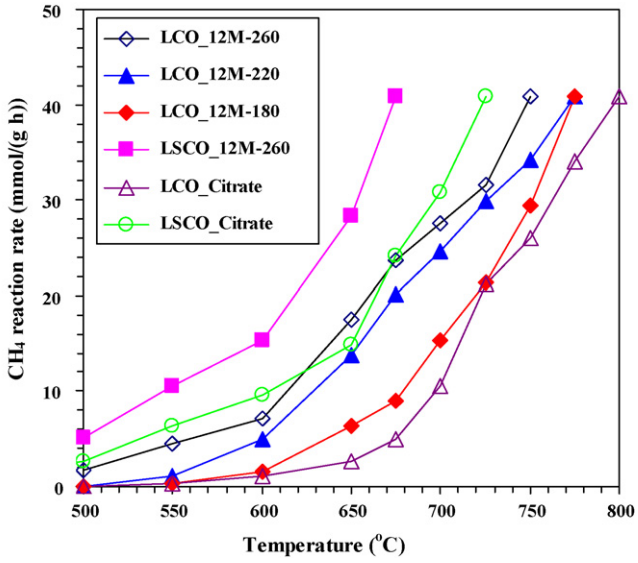


**Fig. 6.** $CH_4$ reaction rate as a function of temperature over the as-fabricated LCO and LSCO catalysts at $CH_4/O_2$ molar ratio = 1/10 and SV = 50,000 mL/(g h).

oxidation over LCO and LSCO was a catalytic process rather than a homogeneous reaction. As shown in Table 1, the $T_{10\%}$, $T_{50\%}$, and $T_{90\%}$ over the LSCO_12M-260 catalyst was much lower than those over the three LCO catalysts, respectively. Fig. 6 shows the methane reaction rate as a function of temperature over the LCO and LSCO catalysts under the conditions of $CH_4/O_2$ molar ratio = 1/10 and SV = 50,000 mL/(g h). It is observed that $CH_4$ reaction rate increased monotonously with increasing temperature, a similar change trend appeared in the plot of methane conversion versus temperature (not shown here); the single-crystalline LSCO_12M-260 and LCO_12M-260 catalysts outperformed the polycrystalline LSCO_Citrate and LCO_Citrate catalysts, respectively. Among all of the catalysts, LSCO_12M-260 showed the best activity ($T_{50\%}$ = 620 °C and $T_{90\%}$ = 667 °C, $CH_4$ reaction rate = 40.9 mmol/(g h) at 667 °C). The catalytic performance decreased according to the order of LSCO_12M-260 ≫ > LCO_12M-260 > LCO_12M-220 > LCO_12M-180. Under similar reaction conditions, the catalytic activity ($T_{50\%}$ = 620 °C and $T_{90\%}$ = 667 °C) over LSCO_12M-260 was much better than those ($T_{50\%}$ = 654 °C and $T_{90\%}$ = 800 °C over $La_{0.9}Cu_{0.1}MnO_3$ [29], $T_{50\%}$ = 710 °C and $T_{90\%}$ = 770 °C over 20 wt.% $LaMnO_3$/MgO [30], $T_{50\%}$ = 620 °C and $T_{90\%}$ = 710 °C over $La_{0.5}Sr_{0.5}MnO_3$ [31]), close to that ($T_{50\%}$ = 600 °C and $T_{90\%}$ = 700 °C over $La_{0.66}Sr_{0.34}Ni_{0.2}Fe_{0.8}O_{3-\delta}$ catalyst [32]), but inferior to those ($T_{50\%}$ = 365 °C and $T_{90\%}$ = 425 °C over 1 wt.% $Pd/ZrO_2$ [33] and $T_{50\%}$ = 520 °C and $T_{90\%}$ = 570 °C over $La_{0.5}Sr_{0.5}MnO_3$ cubes [34]). The discrepancy in catalytic performance of LSCO_12M-260 nanorods and $La_{0.5}Sr_{0.5}MnO_3$ cubes [34] might be related to the differences in crystal structure, oxygen vacancy density, and redox ($Cu^{3+}/Cu^{2+}$ and $Mn^{4+}/Mn^{3+}$) ability as well as particle morphology of the two materials. For comparison purposes, we also measured the catalytic activities of polycrystalline LCO_Citrate and LSCO_Citrate microparticles for methane combustion. The $T_{50\%}$ and $T_{90\%}$ values were 723 and 785 °C over LCO_Citrate, and 660 and 720 °C over LSCO_Citrate, respectively, which were obviously higher than those over LCO_12M-260 and LSCO_12M-260.

As pointed out early, single-crystalline $La_{0.5}Sr_{0.5}MnO_3$ nano-/microcubes [10] and $La_{0.6}Sr_{0.4}CoO_3$ nanowires/nanorods [15] showed better catalytic performance than their polycrystalline irregularly morphological counterparts. It means that the single crystallinity and specific morphology of the perovskite oxides contribute to the enhancement in catalytic performance. Similar effects would also be present in our single-crystalline LCO and LSCO catalysts with a rod-like morphology (Fig. 2). From Table 1, one can find that there was no definite relationship between the surface area and catalytic activity, although the best-performing LSCO_12M-260 sample possessed the highest surface area. For the other three catalysts (LCO_12M-180, LCO_12M-220, and LCO_12M-260), a higher surface area did not lead to a better catalytic activity. Therefore, we believe that surface area was not a key factor influencing the catalytic performance of such a kind of materials. It is well known that oxygen species adsorbed at oxygen vacancies of perovskite-like oxides play an important role in the total oxidation of hydrocarbons. As revealed in the XPS, $O_2$-TPD, and $H_2$-TPR investigations (Table 1 and Figs. 3–5), surface $Cu^{3+}$ content, surface adsorbed oxygen amount, α-oxygen desorption, and reducibility on/of the LSCO_12M-260 catalyst were higher than those on/of the LCO catalysts, and followed a sequence of LSCO_12M-260 ≫ LCO_12M-260 > LCO_12M-220 > LCO_12M-180, which was the same order in catalytic performance (Table 1 and Fig. 6). Therefore, we conclude that more adsorbed oxygen species, better reducibility, single crystallinity, and unique morphology are responsible for the excellent performance of the hydrothermally fabricated LSCO_12M-260 catalyst for methane combustion.

## 4. Conclusion

By adopting the hydrothermal strategy with KOH as the alkaline source, one could generate microrod-like single-crystalline LCO and LSCO with perovskite-like structures after a high-temperature calcination process. It is shown that the LCO catalysts possessed an orthorhombic perovskite-like structure whereas the LSCO catalyst exhibited a tetragonal perovskite-like structure. All of the single-crystalline cuprates had a relative low surface area of 3.6–11.9 $m^2$/g, and there was no direct relation between the surface area and catalytic activity. The single-crystalline LSCO catalyst was superior in performance to its polycrystalline counterpart. The partial substitution of $La^{3+}$ by $Sr^{2+}$ gave rise to an enhancement in catalytic activity of the parent $La_2CuO_4$ material. Under the conditions of $CH_4/O_2$ molar ratio = 1/10, SV = 50,000 mL/(g h), the hydrothermally fabricated LSCO_12M-260 catalyst showed the best performance ($T_{50\%}$ = 620 °C and $T_{90\%}$ = 667 °C) for methane combustion. The characterization results indicate the presence of a clear relationship between the α-oxygen desorption or reducibility and catalytic performance. We believe that the excellent activity of the single-crystalline $LaSrCuO_4$ catalyst for methane combustion are intimately associated with the factors such as more adsorbed oxygen species, better reducibility, single crystallinity, and unique morphology.

## Acknowledgments

This work was supported by the NSF of China (Grant No. 20973017), the Creative Team of Beijing Municipality (Grant No. PHR200907105), and NSF of Beijing Municipality (Key Class B project of Grant No. KZ200610005004).

## References

[1] S. Royer, C. Ayrault, C. Carnevillier, F. Epron, P. Marécot, D. Duprez, Catal. Today 117 (2006) 543–548.
[2] G.L. Flem, G. Demazeau, P. Hagenmuller, J. Solid-State Chem. 44 (1982) 82–88.
[3] M. Al Daroukh, V.V. Vashook, H. Ullmann, F. Tietz, I. Arual Raj, Solid-State Ionics 158 (2003) 141–150.
[4] H.X. Dai, C.F. Ng, C.T. Au, J. Catal. 197 (2001) 251–266.
[5] A.K. Ladavos, P.J. Pomonis, J. Chem. Soc., Faraday Trans. 87 (1991) 3291–3297.
[6] S. Ifrah, A. Kaddouri, P. Gelin, D. Leonard, C.R. Chimie 10 (2007) 1216–1226.
[7] Y. Mao, S. Banerjee, S.S. Wong, Chem. Commun. (2003) 408–409.
[8] J. Miao, C.G. Hu, H. Liu, Y.F. Xiong, Mater. Lett. 62 (2008) 235–238.
[9] Y.W. Wang, H. Xu, X.B. Wang, X. Zhang, H.M. Jia, L.Z. Zhang, J.R. Qiu, J. Phys. Chem. B 110 (2006) 13835–13840.
[10] F. Teng, W. Han, S.H. Liang, B. Gaugeu, R.L. Zong, Y.F. Zhu, J. Catal. 250 (2007) 1–11.
[11] H.X. Dai, H. He, W. Li, Z.Z. Gao, C.T. Au, Catal. Lett. 73 (2001) 149–156.
[12] H.X. Dai, H. He, P.H. Li, L.Z. Gao, C.T. Au, Catal. Today 90 (2004) 231–244.
[13] H.X. Dai, C.F. Ng, C.T. Au, J. Catal. 189 (2000) 52–62.
[14] H.X. Dai, C.F. Ng, C.T. Au, J. Catal. 193 (2000) 65–79.
[15] J.G. Deng, L. Zhang, H.X. Dai, H. He, C.T. Au, Catal. Lett. 123 (2008) 294–300.
[16] J.R. Niu, J.G. Deng, W. Liu, L. Zhang, G.Z. Wang, H.X. Dai, H. He, X.H. Zi, Catal. Today 126 (2007) 420–429.
[17] J.G. Deng, L. Zhang, H.X. Dai, H. He, C.T. Au, J. Mol. Catal. A 299 (2009) 60–67.
[18] J.J. Zhu, Z. Zhao, D.H. Xiao, J. Li, X.G. Yang, Y. Wu, J. Mol. Catal. A 238 (2005) 35–40.
[19] M.W. Roberts, Chem. Soc. Rev. 18 (1989) 451–475.
[20] R. Polini, A. Falsetti, E. Traversa, O. Schäf, P. Knauth, J. Eur. Ceram. Soc. 27 (2007) 4291–4296.
[21] J.H. Li, H.J. Fu, L.X. Fu, J.M. Hao, Environ. Sci. Technol. 40 (2006) 6455–6459.
[22] J.H. Choy, D.Y. Jung, S.J. Kim, Q.W. Choi, G. Demazeau, Physica C 185–189 (1991) 763–764.
[23] C.-H. Wang, C.-L. Chen, H.-S. Weng, Chemosphere 57 (2004) 1131–1138.
[24] S. Kaliaguine, A. Van Neste, V. Szabo, J.E. Gallot, M. Bassir, R. Muzychuk, Appl. Catal. A 209 (2001) 345–358.
[25] S. Royer, H. Alamdari, D. Duprez, S. Kaliaguine, Appl. Catal. B 58 (2005) 273–288.
[26] S. Petrović, A. Terlecki-Baričević, L. Karanović, P. Kirilov-Stefanov, M. Zdujić, V. Dondur, D. Paneva, I. Mitov, V. Rakić, Appl. Catal. B 79 (2007) 186–198.
[27] Z.-B. Chen, T.-R. Ling, M.-D. Lee, React. Kinet. Catal. Lett. 62 (1997) 185–190.
[28] J. Liu, Z. Zhao, C.M. Xu, A.J. Duan, Appl. Catal. B 78 (2008) 61–72.
[29] G. Bulgan, F. Teng, S.H. Liang, W.Q. Yao, Y.F. Zhu, Acta Phys. Chim. Sin. 23 (2007) 1387–1392.
[30] E.E. Svensson, S. Nassos, M. Boutonnet, S.G. Järås, Catal. Today 117 (2006) 484–490.
[31] S. Ponce, M.A. Peña, J.G.L. Fierro, Appl. Catal. B 24 (2000) 193–205.
[32] M. Alifanti, J. Kirchnerova, B. Delmon, D. Klvana, Appl. Catal. A 262 (2004) 167–176.
[33] S. Guerrero, P. Araya, E.E. Wolf, Appl. Catal. A 298 (2006) 243–253.
[34] S.H. Liang, F. Teng, G. Bulgan, Y.F. Zhu, J. Phys. Chem. C 111 (2007) 16742–16749.